


Pressure Sensor Using a Hybrid Structure of a Magnetostrictive Layer and Nitrogen-Vacancy Centers in Diamond

Ryota Kitagawa¹, Shunsuke Nagata¹, Keigo Arai^{1,2}, Kosuke Mizuno¹, Takeyuki Tsuji¹,
Ikuya Fujisaki¹, Soki Urashita¹, Teruo Kohashi³, Yota Takamura¹, Takayuki Iwasaki¹,
Shigeki Nakagawa¹ and Mutsuko Hatano^{1,*}

¹*School of Engineering, Tokyo Institute of Technology, 2-12-1 Ookayama, Meguro-ku, Tokyo, 152-8550, Japan*

²*PRESTO, Japan Science and Technology Agency (JST), 7 Gobancho, Chiyoda-ku, Tokyo, 102-0076, Japan*

³*Center for Exploratory Research, Research & Development Group, Hitachi, Ltd., 2520 Akanuma, Hatoyama, Saitama, 350-0395, Japan*

 (Received 1 July 2022; revised 18 March 2023; accepted 23 March 2023; published 27 April 2023)

This study demonstrates imaging of the magnetic response to external pressure using a hybrid structure of magnetostrictive (MS) layers and nitrogen-vacancy (N-V) centers in diamonds. The MS layer facilitates pressure-to-magnetic field conversion, detected by N-V centers. We use hybrid materials comprising in-plane magnetized SmFe₂ as a MS layer and diamond with N-V centers perfectly aligned in the vertical [111] orientation to effectively detect the pressure-to-magnetic field conversion. The pressure coefficient, defined as the change in the resonant frequency of the optically detected magnetic resonance in response to pressure, is imaged by widefield imaging, while varying the pressure applied to the MS-N-V structure. We observe a pressure-dependent change in the resonant frequency. Through widefield imaging, the pressure coefficients are found to be correlated with the multidomain structure of the MS layer, which must be considered in widefield pressure imaging. The highest pressure coefficient is 8.2 kHz kPa⁻¹ in a domain—550 times greater than that achieved by a single structure of the N-V center. We propose and discuss the approach of using MS disk arrays consisting of a single domain to improve the sensitivity and controllability and to enable accurate calibration of pressure imaging.

DOI: [10.1103/PhysRevApplied.19.044089](https://doi.org/10.1103/PhysRevApplied.19.044089)

I. INTRODUCTION

Nitrogen-vacancy (N-V) centers in diamonds are used as highly sensitive magnetic field [1–6], temperature [7], electric field [8], and pressure sensors [9,10]. As for pressure sensors, nanomechanical sensing towards mass spectrometry and force microscopy are demonstrated [9]. Moreover, the N-V center ensemble allows pressure imaging with high spatial resolution on the submicrometer scale, which is restricted by the diffraction limit of light. This feature is used to image the pressure tensor of diamond crystals in high-pressure environments [10].

Improving pressure sensitivity is the key to expanding the application of N-V centers as pressure sensors. The current implementation of pressure sensing using N-V centers is based on the fact that strain induces a change in the magnitude of dipole interactions between electron spins in N-V centers, which changes the resonant frequency of electron spins detected by optically detected magnetic resonance (ODMR). The change in resonant frequency per unit pressure is typically 14.6 Hz kPa⁻¹ under

hydrostatic pressure [11]. This pressure coefficient of the N-V center is limited by the amount of deformation of the diamond lattice in response to pressure [12]. A more efficient change in the resonant frequency per pressure, based on different physics, improves the pressure sensitivity of N-V centers. Such highly sensitive pressure sensing combined with nanoscale [13,14] and/or widefield imaging [15,16] will pave the way for different applications, such as weight dynamics imaging of live cells, which is correlated with the underlying mechanisms of cellular growth [17,18]. Moreover, the simultaneous realization of high-pressure sensitivity, high spatial resolution, and wide measurement range will be an improvement over the currently established pressure-imaging methods [19,20].

Theoretical calculations performed by Cai *et al.* showed that a hybrid structure of magnetostrictive (MS) material and N-V centers was a promising candidate [21]. In the hybrid structure, the pressure applied to the MS layer changes the magnetic anisotropy through the inverse MS effect, rotates the magnetization, and changes the stray field of the MS layer. The change in the stray field is then detected by the N-V center using ODMR. In the hybrid structure, the pressure coefficient is limited by the

*hatano.m.ab@m.titech.ac.jp

pressure-to-magnetic field conversion efficiency of the MS layer and the gyromagnetic ratio of the N-V center. Based on their theoretical estimation, the change in the resonant frequency of N-V centers due to pressure is expected to be almost linear up to several MPa and reach the order of 10 kHz kPa⁻¹. This value is 3 orders of magnitude larger than that realized using a single structure of the N-V center. However, such pressure sensing using the MS-N-V hybrid structure is yet to be experimentally demonstrated.

Here, we image a pressure-induced change in the resonant frequency using the MS-N-V hybrid structure and reveal a correlation between the pressure coefficient and the multidomain structure of the MS thin film. This is realized using a hybrid system, in which the MS layer is placed above the N-V center. We employ materials with properties appropriate for pressure-sensitivity improvement for the MS layer and ensemble N-V centers in diamond. As a MS material, we use in-plane magnetized SmFe₂ [22] to convert the pressure into a magnetic field with high efficiency. As a N-V center, we use [111] perfectly aligned N-V centers [23,24] because they are effective to measure the magnetic field along the perpendicular direction for detecting the change in the magnetic field owing to pressure-induced rotation of magnetization. The pressure is applied to the hybrid system using calibrated weights. The change in the resonant frequency of N-V centers is imaged as a function of pressure using a charge-coupled-device (CCD) camera. We successfully observe a pressure-dependent change in the resonant frequency. Widefield imaging reveals that the pressure coefficient is correlated with the multidomain structure of the MS layer; the coefficient is relatively large in the interior of the domain and small near the domain

wall. The maximum coefficient is observed in a domain, and the value is (8.2 ± 0.9) kHz kPa⁻¹, which is 550 times larger than that of a single structure of the N-V center. Furthermore, we propose and discuss the approach of using MS disk arrays consisting of a single domain to improve the sensitivity and controllability and to ensure accurate calibration of pressure imaging.

II. STRUCTURE AND PRINCIPLE OF PRESSURE SENSORS

Imaging of the magnetic response to external pressure is performed using a hybrid structure in which the MS layer is placed above the N-V layer [Fig. 1(a)]. Here, the N-V center is sensitive to the magnetic field of the component along the axis connecting the nitrogen atom and vacancy. The green laser and microwaves, which are necessary for magnetic field measurements using N-V centers, are irradiated from the bottom surface to the N-V centers. The fluorescence of the N-V center is emitted from the underside of the diamond substrate and detected using a CCD camera.

The pressure-to-magnetic field conversion is based on the pressure-induced rotation of magnetization toward the direction of the maximum principal pressure [Fig. 1(b)]. The direction of magnetization in magnetic materials is determined by the minimum point of the sum of the magnetic anisotropy potentials generated by various factors, such as the shape of the magnetic material, crystal structure, and pressure [25]. Here, the magnetic anisotropy potential is represented as a function of the magnetization angle. Pressure causes magnetic anisotropy, depending on

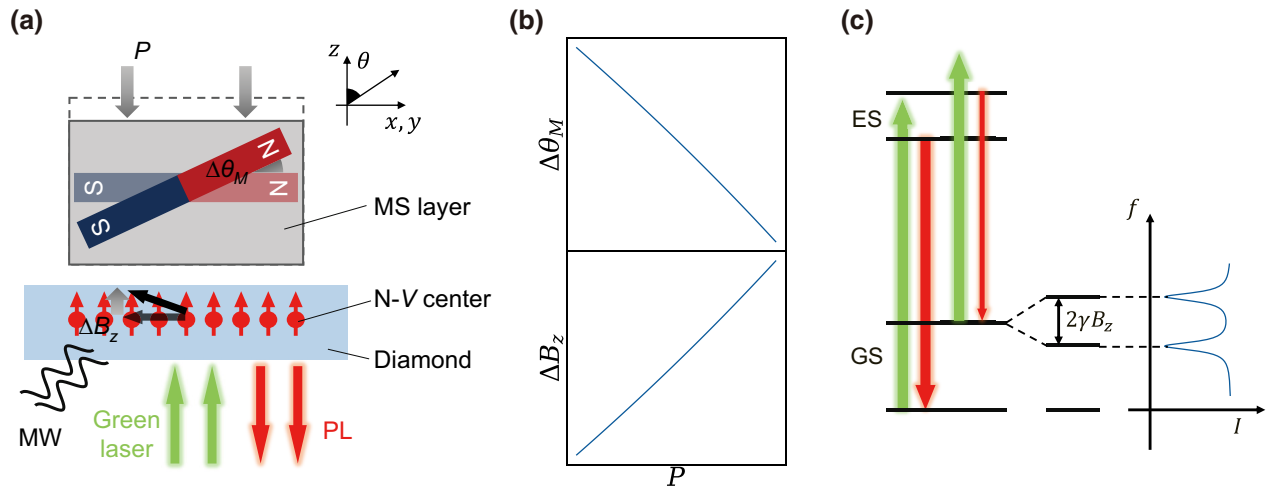


FIG. 1. Detection of the pressure-induced change in magnetic field using the MS-diamond hybrid structure. (a) Overview of the hybrid structure. MS layer is placed above the N-V layer. Pressure applied to the MS layer induces magnetization rotation in the MS layer, changing the magnetic field detected by N-V centers. (b) Pressure-to-magnetic field conversion using the MS layer. Magnetization in the MS layer rotates owing to pressure, changing its z component of the stray field. (c) Magnetic field detection by N-V centers. Change in energy level owing to the magnetic field is detected by ODMR. ES corresponds to excited state; GS corresponds to ground state.

its magnitude and direction, owing to the inverse MS effect.

$$E_{\text{pressure}}(\theta) = -\frac{3}{2}\lambda\sigma \sin^2\theta, \quad (1)$$

where λ , σ , and θ are the MS constant, magnitude of pressure, and the relative angle between the direction of the maximum principal pressure and magnetization, respectively. The direction of anisotropy is determined by the sign of λ and the direction of the maximum principal pressure. For example, when $\lambda < 0$ and compressive pressure is applied, anisotropy occurs in the direction of the maximum principal pressure.

Pressure-induced changes in the magnetic field are detected as changes in the resonant frequency, detected by optical means, by the N- V center [26] [Fig. 1(c)]. The resonant frequency of the N- V center is $D_{\text{GS}} \pm \gamma B_z$ when the magnetic field in the x and y directions, pressure, and electric field are negligible. Here, $D_{\text{GS}} \sim 2.87$ GHz is the zero-field-splitting term [7, 11, 12, 26]. γ (28 MHz mT $^{-1}$) is the gyromagnetic ratio of electron spin in the N- V center [27]. The z direction connects nitrogen and vacancies in the N- V center. Microwaves (MWs) with a frequency equal to the resonant frequency cause resonance and change the spin state of the N- V center. The change in spin state is read as a change in the intensity of red photoluminescence when irradiated with laser light with a wavelength of 532 nm [28, 29]. When the MW frequency is swept while irradiating the laser, the fluorescence intensity changes only when the MW frequency matches the resonant frequency [26].

In the hybrid system, the pressure coefficient is determined by the magnetic properties of the MS material, dimensional properties, and the gyromagnetic ratio of the N- V center. The essential magnetic properties are the MS constant, magnetic moment density, and initial magnetic anisotropy. Each factor has an approximately linear influence on the pressure coefficient. The dimensional properties include the distance between the N- V and MS layers and the size of the magnetic domain. Magnetic fluxes mainly originate from domain edges; thus, the aspect ratio of the standoff distance and size of the domain is essential. The gyromagnetic ratio is a function of the g factor of electron spin in the N- V centers; however, it is approximately constant for sensing based on N- V centers (28 MHz mT $^{-1}$ [6]).

III. EXPERIMENTAL METHOD

We measure the change in the resonant frequency of N- V centers while varying the pressure applied to the MS layer. We apply pressure to the hybrid system using a calibrated weight through a rivet with a diameter of 2 mm. The pressure magnitude is varied by changing the number of calibrated weights. The weights vary from 0 to 20 g. We confirm that the weight is correctly applied using an

electronic balance (see Appendix A). We insert a 0.5-mm-thick layer of urethane gel to ensure spatial uniformity of the pressure, primarily used as the cushioning material, between the bottom of the rivet and MS layer. The pressure is assumed to be uniform within the field of view (FOV) and calculated by dividing the weight by the bottom area of the rivet ($\pi \times 1 \times 1$ mm 2); thus, the pressure is varied between 0 and 62 kPa. Note that this procedure has a certain systematic error: part of the rivet protrudes from the diamond and raises by 30 μ m only at the MS thin film, and the bottom of the rivet is not completely flat. We use SmFe $_2$, which is expected to exhibit a high pressure-to-magnetic field conversion efficiency, as the MS material [22, 30]. We employ facing-target sputtering to deposit SmFe $_2$ thin films with a thickness of 100 nm on 30- μ m-thick glass substrates. Before incorporating SmFe $_2$ into the hybrid system, SmFe $_2$ is magnetically saturated by applying a strong magnetic field sufficient for saturation (> 1 T) in the in-plane direction, which is the easy axis of magnetization. A perpendicular bias magnetic field of approximately 2 mT is applied to the entire system using a permanent magnet to resolve the degeneracy of the N- V center. The effect of the perpendicular magnetic field on the magnetic properties of SmFe $_2$ is negligible, based on the magnetization characteristics of SmFe $_2$ [Fig. 2(b)].

We evaluate the fundamental magnetic properties of SmFe $_2$. First, we evaluate the magnetic anisotropy and MS properties using a vibrating sample magnetometer to validate that the deposited SmFe $_2$ films have sufficient properties for highly efficient pressure-to-magnetic field conversion. The magnetic anisotropy is evaluated by measuring the magnetization-magnetic field (M - H) hysteresis curves in the in-plane (blue) and out-of-plane (green) directions [Fig. 2(b)]. SmFe $_2$ exhibits in-plane magnetic anisotropy; the in-plane direction requires less magnetic field to reach saturation magnetization and has a larger remanent magnetization than the out-of-plane direction. The in-plane-magnetized MS film and [111] perfectly aligned N- V centers allow the efficient detection of pressure-magnetic field conversion. Additionally, we evaluate the MS properties by measuring the M - H hysteresis curve while applying pressure. The MS constant, λ , is estimated from the change in anisotropic energy versus bending pressure and $\lambda = (-900 \pm 50)$ ppm is obtained. The obtained MS constant can be compared with the value of $|\lambda|$, which is approximately 2000 ppm for general MS materials.

Second, to ensure magnetic field images obtained by N- V centers undoubtedly originate from the SmFe $_2$ layer and to examine the distribution of the pressure coefficient, we observe a magnetic domain structure using magneto-optical Kerr effect (MOKE) imaging [Fig. 2(c)]. A longitudinal MOKE image is shown in Fig. 2(c); the contrast reflects the magnetization distribution in the in-plane direction. Stripelike magnetic domains with

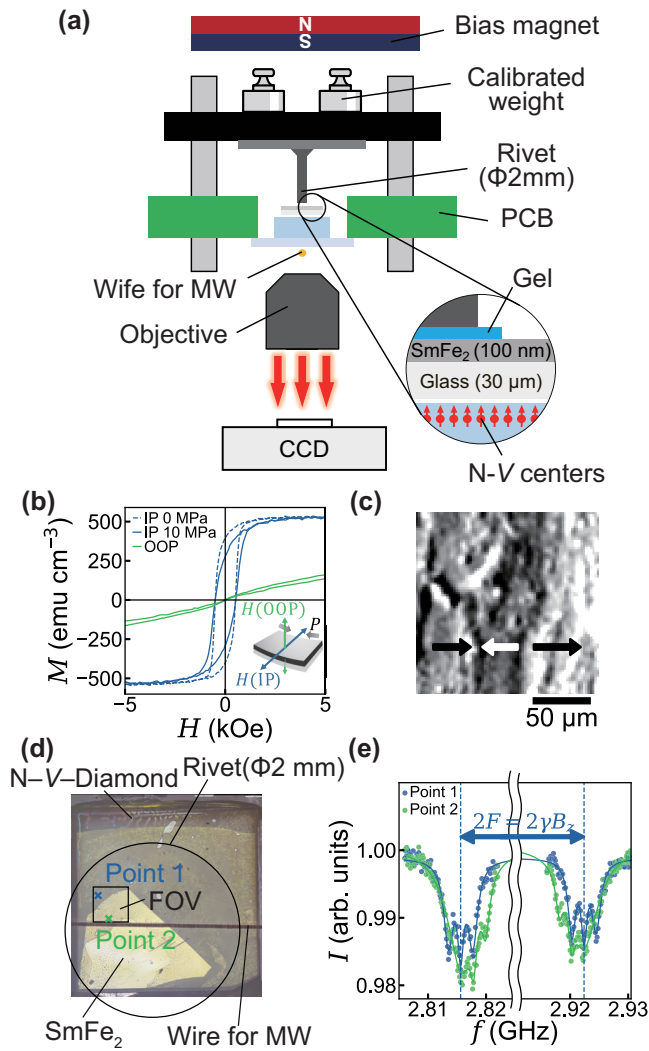


FIG. 2. (a) Experimental setup for imaging of the magnetic response to external pressure using a hybrid structure of the MS layer and N- V centers in diamond. Pressure is applied by a calibrated weight through a rivet with a diameter of 2 mm into SmFe₂, a MS material. Gel is placed between the SmFe₂ layer and foot of the rivet to homogenize the pressure. Bias magnet is placed above the calibrated weights. Thickness of the SmFe₂ layer is 100 nm and the distance between SmFe₂ and N- V centers is at least 30 μ m, which is the thickness of the glass substrate. CCD camera images photoluminescence from N- V centers. (b) M - H hysteresis loop of the SmFe₂ layer along the in-plane (IP) and out-of-plane (OOP) directions. SmFe₂ has an in-plane magnetic anisotropy and MS constant of $\lambda = (-900 \pm 50)$ ppm. (c) Magnetization image of SmFe₂ obtained by MOKE imaging. Black and white arrows show the magnetization directions. We adjust the color map for contrast enhancement and employ a blurring process for smoothing. Scale bar is 50 μ m. (d) Optical image of the setup. Circle is the foot of the rivet and the square is the FOV of the magnetic field image. (e) ODMR spectrum of the [111] perfectly aligned N- V layer. Magnetic field is determined by the difference in the two resonant frequencies.

widths of approximately 75 μ m are observed. This domain structure induces the distribution of the magnetic field and pressure coefficient on a scale similar to the domain structure.

To detect the pressure-induced change in the magnetic field, it is effective to measure the magnetic field along the direction perpendicular to the N- V -surface plane as aforementioned. Thus, we use [111] perfectly aligned N- V centers deposited by chemical vapor deposition on Ib diamond (111) substrates [23,24,31]. The N- V center layer is successfully oriented along the [111] direction [Fig. 2(e)]. The thickness of the N- V layer estimated using secondary-ion mass spectrometry analysis is approximately 10 μ m [31].

The magnetic fields at the N- V centers are imaged in parallel using a CCD camera [32]. The FOV for magnetic field imaging is designed to include both areas with and without SmFe₂ and to be inside the foot of the rivet [Fig. 2(d)]. The area is 375 \times 375 μ m² with a pixel size of 4.9 μ m, which is sufficient to comprehensively observe the magnetic domain. Note that the effective spatial resolution is greater than 4.9 μ m because the thickness of the N- V centers is 10 μ m, which is larger than the pixel size, and the N- V -sample standoff distance is >30 μ m [33]. The spatial resolution is ultimately limited by optical diffraction, which is characterized by the wavelength (\sim 700 nm) and the numerical aperture (0.15 in our experiment using Olympus MPLFLN5X). Continuous-wave ODMR imaging is used for magnetic field imaging. Each magnetic field image is obtained by integration over 30 min. The split width of the ODMR peaks, which corresponds to the strength of the magnetic field, differs between areas without [point 1 in Fig. 2(e)] and with (point 2) SmFe₂, which indicates that the stray field from the SmFe₂ layer is detected. The magnetic field along the [111] direction is obtained by fitting the ODMR peak with six Lorentzian functions [34] and dividing the difference in the resonant frequencies of the second and fifth peaks, $2F$, by twice the gyromagnetic ratio. The magnetic field varies by approximately 0.3 mT, depending on the location.

During ODMR measurements, the entire FOV drifts randomly in the x - y direction. This x - y directional drift makes it challenging to observe pressure-induced changes in the magnetic field. Thus, we perform subpixel drift correction using the phase-limited correlation method [35,36]; we correct the drift using the characteristic geometry in the bright-field image as a reference. We ensure that the artificially generated drift is corrected within an error of approximately 0.4 pixels (2 μ m). A drift of 0.4 pixels produces a change in the resonant frequency of the N- V center of approximately \pm 200 kHz. The change in the resonant frequency obtained in this study exceeds \pm 200 kHz; therefore, the change originates from factors other than the drift.

IV. RESULTS AND DISCUSSION

We observe changes in the resonant frequency that exceed the estimation error and effect of the x - y directional drift (Fig. 3). The magnetic field image at $P = 0$ kPa is shown in Fig. 3(a). The differences in the resonant frequencies, $\Delta F = \gamma \Delta B_z$, from 0 kPa at 31 and 62 kPa are shown in Figs. 3(b) and 3(c). On average, the estimation error of ΔF is $1\sigma = 38$ kHz. Note that a change in the resonant frequency of 2.3 kHz kPa $^{-1}$, which may originate from an experimental artifact, is eliminated during data processing (see Appendix B). When the pressure is applied, ΔF shows both positive and negative signs in the region of SmFe $_2$ [Figs. 3(b) and 3(c)]. Moreover, the absolute value of ΔF increases as the applied pressure increases.

We map the pressure coefficient by fitting the pressure-resonant-frequency dependence using a linear function pixel by pixel and extracting the gradient to systematically investigate the pressure-resonant-frequency conversion behavior [Fig. 3(d)]. An example of the linear fit is shown in Fig. 3(e). The selected point is shown as the origin of the arrow running between Figs. 3(d) and 3(e). In Fig. 3(e), the horizontal axis represents the pressure calculated from the calibrated weight and the area of the bottom of the rivet, and the vertical axis represents the change in the ODMR split width, F , of the N- V centers from 0 kPa. Horizontal error bars are pressure-calibration errors (see Appendix A) and vertical error bars are $\pm 1\sigma$ confidence intervals. We use the weighted least-squares method, where the confidence interval of ΔF at each pressure is considered, and only the gradient is a free parameter. The solid line represents the result of the linear fit. Based on theoretical calculations that assume a single-domain MS cube, the change in resonant frequency as a function of pressure is approximately linear, up to a few MPa [21]. However, because we use the extended thin film, the dependence in our experiments can be more complex: domain-wall motion, the interaction between domains, and impurity in the film can influence the characteristics. Thus, the linear fit is only indicative of an approximate dependence. The estimation error of the pressure coefficient is $1\sigma = 0.46$ kHz kPa $^{-1}$ on average. The pressure coefficients are distributed over both positive and negative signs. The spacing of the points with pressure coefficients of zero is approximately 75 μm , which is close to the domain width. The distribution of pressure coefficients correlates with the distribution of the domain structure.

We examine the correlation between the pressure coefficient and the domain structure. The domain structure in the in-plane magnet, where the magnetization faces the domain wall, as shown in Fig. 2(c), can be estimated from the position of the domain wall, where the perpendicular component of the magnetic flux density is large [Fig. 3(g)]. The position of the domain wall estimated by eye is partially shown as black dashed lines and that of the domain

is partially shown as green ovals in Figs. 3(a) and 3(d), respectively. The interval of the domain wall is approximately 75 μm , which is consistent with magnetization mapping obtained by MOKE [Fig. 2(c)]. The magnetic field image and the pressure-coefficient image are cropped at specific line segments to compare the domain structure and the pressure-coefficient distributions [Fig. 3(f)]. The cutout location is indicated by the black solid lines in Figs. 3(a) and 3(d). The two graphs in Fig. 3(f) have a common horizontal axis, with the position relative to the leftmost point. The vertical axes represent the magnetic field and pressure coefficient. The gray area shows the $\pm 1\sigma$ confidence interval. The black vertical dashed lines in the two graphs represent the maxima and minima of the magnetic field distribution, which correspond to the positions of the domain walls. The pressure coefficient has a distribution that depends on the domain structure, with positive or negative values in the domain and approximately zero on the domain wall. Such a distribution of the pressure coefficient should be considered toward pressure imaging. Moreover, the highest pressure coefficient is observed in a domain and the value is (8.2 ± 0.9) kHz kPa $^{-1}$, which is 550 times larger than that realized by the N- V center alone [Fig. 3(d)].

The reason for the pressure-coefficient distribution remains unknown. A possible reason is that the direction of magnetization rotation differs between domains. Such a phenomenon can occur because pressure-induced anisotropy is uniaxial anisotropy; magnetization rotates towards the $+z$ or $-z$ direction [Fig. 3(h)]. In that case, in a domain, the stray field from the nearest domain will be dominant and B_z will increase or decrease, depending on the direction of magnetization rotation. On a domain wall, the change along the z direction is small (similar to the derivative of the cosine function near zero) and the effect of two neighboring domains is canceled out, so changes in the magnetic field will not be observed. A more detailed understanding can be provided when considering broken symmetry, the energy stored in the domain wall, and domain-wall motion. In addition, magnetic imaging with nanoscale spatial resolution allows elucidation of a detailed mechanism.

We demonstrate a pressure-dependent change in the resonant frequency of the MS-N- V hybrid structure. Wide-field imaging reveals that the pressure coefficients are correlated with the multidomain structure of the MS layer, which must be considered in widefield pressure imaging. Some challenges must be overcome to apply the MS-N- V hybrid structure to pressure sensors, such as accurate calibration and improvement of controllability and sensitivity.

First, we examine the calibration of the MS-N- V hybrid sensor. The simplicity of the resonant-frequency-pressure characteristics is essential for sensor calibration. We investigate the characteristics classifying them into in-domain or on-domain-wall regions. We select several points in

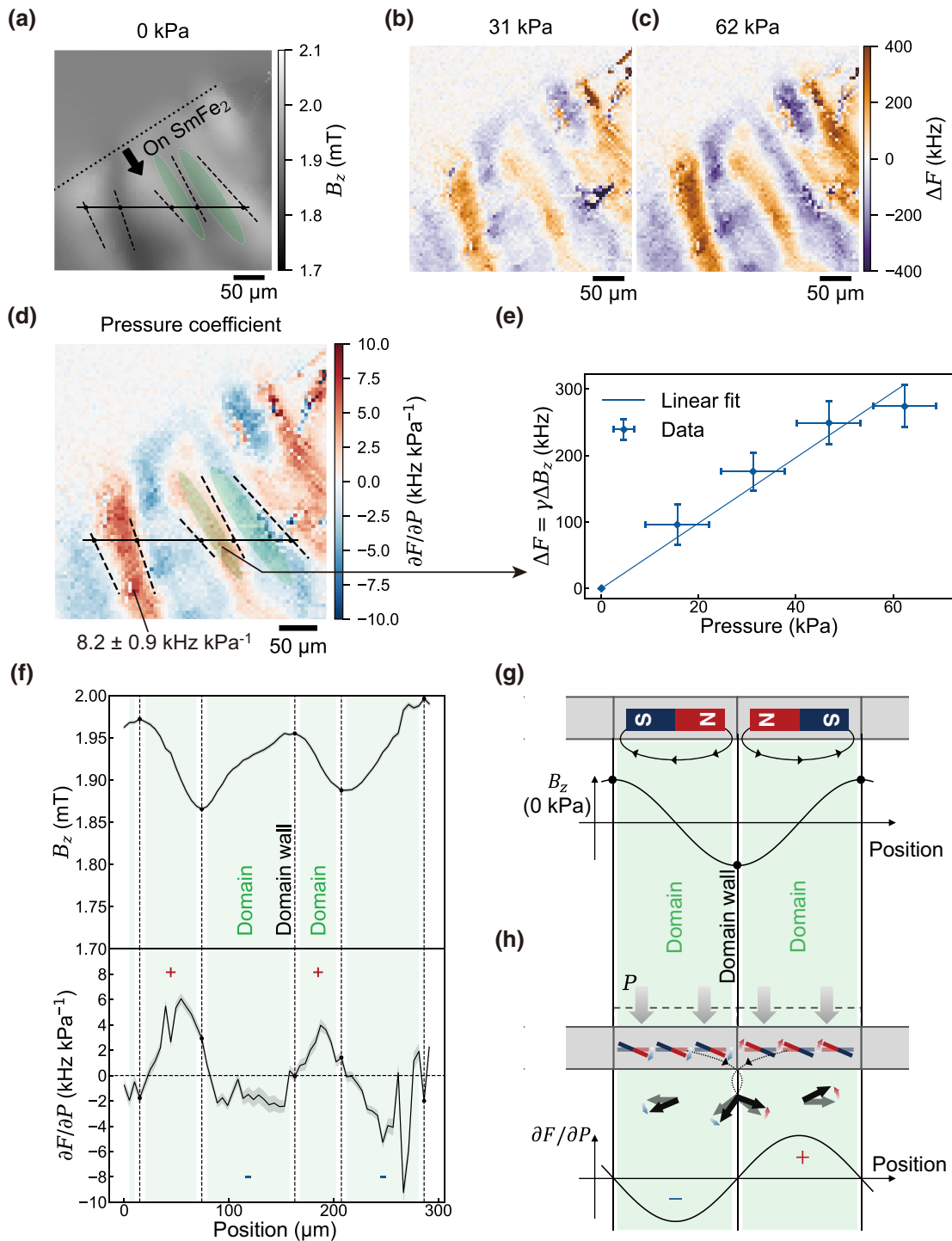


FIG. 3. Imaging of the magnetic response to external pressure using a MS–N– I hybrid structure. (a) Magnetic field image at $P=0$. SmFe_2 thin film has a multidomain structure. Black dashed lines and green shading represent the rough position of domain walls and domains estimated by eye, respectively. (b),(c) Changes in the resonant frequency owing to pressure at 31 and 62 kPa. (d) Distribution of the pressure coefficient. Black dashed lines and green shading are plotted in the same position as in (a). Maximum pressure coefficient is (8.2 ± 0.9) kHz kPa $^{-1}$. (e) Example of the linear fit used in (d). (f) Line cut of the magnetic field and coefficient. Cutout location is indicated by the line segments in (a),(d). Pressure coefficients are correlated with the multidomain structure of the MS layer. (g) Schematic of an explanation that the maxima or minima of B_z distributions correspond to a domain wall. (h) Model to understand the distribution of the pressure coefficient. Scale bar is 50 μ m in all images.

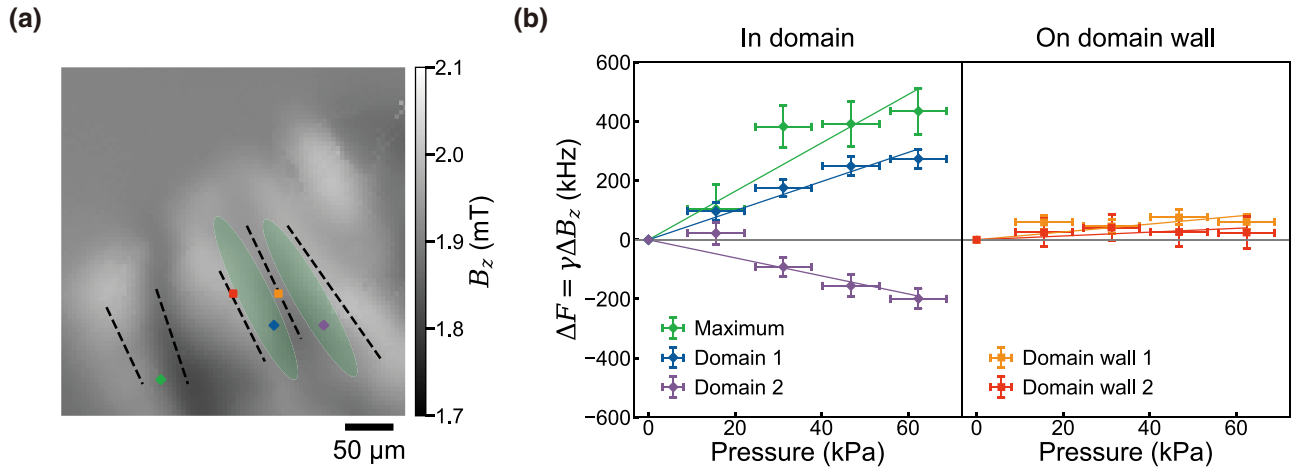


FIG. 4. (a) Magnetic field image at $P = 0$ kPa to determine the position of domains. Scale bar is 50 μm . (b) Pressure-induced change in the resonant frequency. Solid line represents a linear fit. Selected points are shown in (a).

the domain (blue and purple), on the domain wall (red and orange), and where the pressure coefficient is maximum (green) [Fig. 4(a)]. The resonant-frequency–pressure characteristics are shown in Fig. 4(b). Some of the points in Fig. 4(b) agree with the linear fit. Some points exhibit nonmonotonic resonant-frequency–pressure characteristics (purple), suggesting the presence of oppositely rotating magnetic domains or defects. For pressure sensors, nonlinear dependence and the spatial distribution of the pressure coefficients make calibration difficult. Investigating the factors behind the nonlinearity and resolving them will be the subject of future work. Measurements with higher spatial resolution than those obtained in this experiment, such as a $N-V$ -based scanning probe [37], are expected to lead to elucidation of the mechanism. Moreover, the resonant-frequency–pressure characteristics are simplified by using a single-domain MS magnet, similar to theoretical predictions [21].

Second, we examine control of the domain structure. We use an extended thin film that has a multidomain structure [Fig. 5(a)] and each domain corresponds to one pixel for pressure imaging. Controlling the domain structure is necessary for more advanced pressure imaging. In particular, it is essential to eliminate magnetic-domain-size variation, suppress domain-wall motion, and ensure the reproducibility of the domain structure. Such improvements can be achieved by single-domain nano- or micro-MS arrays [Fig. 5(b)]. Each MS disk is expected to become a single domain by processing them down to the microscale [38]. The precision of device fabrication limits the size variation of MS disks, and each disk is expected to be processed into dimensions of sufficiently high accuracy. Magnetic domain motion is quite unlikely to occur. Reproduction of the domain structure can be achieved by saturating the magnetization with an external magnetic field.

We demonstrate MS disk arrays consisting of a single domain. A 100-nm-thick SmFe_2 film deposited on a thermally oxidized silicon substrate is processed into a 60- μm -diameter disk array by argon-ion milling [Fig. 5(c)]. We image the stray-field distribution to validate the domain structure of the SmFe_2 disk. An ensemble $N-V$ center fabricated on a diamond IIa substrate (100) is placed directly above the SmFe_2 disks. The $N-V$ center has four crystallographic orientations, which enable us to perform magnetic field vector imaging. The thickness of the $N-V$ center is 50 nm. The spatial resolution for magnetization distribution is limited by the standoff distance between the SmFe_2 disk and $N-V$ layer, which is expected to be several micrometers. The three components of the magnetic field vector are imaged for a particular disk [Fig. 5(d)]. As revealed by the magnetic field distribution, the MS disk is a single-domain magnet; the disk has one outpouring (inpouring) of magnetic flux, which corresponds to the N (S) pole. The interval and size of the MS disks can be optimized in the future toward pressure imaging.

Third, we examine the improvement in the pressure coefficient. As mentioned earlier, the pressure-to-magnetic field conversion efficiency is determined by the magnetic and geometric properties of the MS material. The pressure coefficient can be effectively increased in terms of magnetic properties by weakening the magnetic anisotropy and increasing the MS constant. In terms of geometric properties, the pressure coefficient can be effectively increased by shortening the distance between the MS and $N-V$ layers because the magnetic field intensity at the $N-V$ center increases as the distance decreases. The distance between the MS and $N-V$ layers is >30 μm in the experiment shown in Figs. 3 and 4 and shorter in Fig. 5 (~ 15 μm , estimated by magnetization reconstruction, where the standoff distance is included in the free parameters). The amplitude of the magnetic field changes from ± 0.15 mT [Fig. 3(a)]

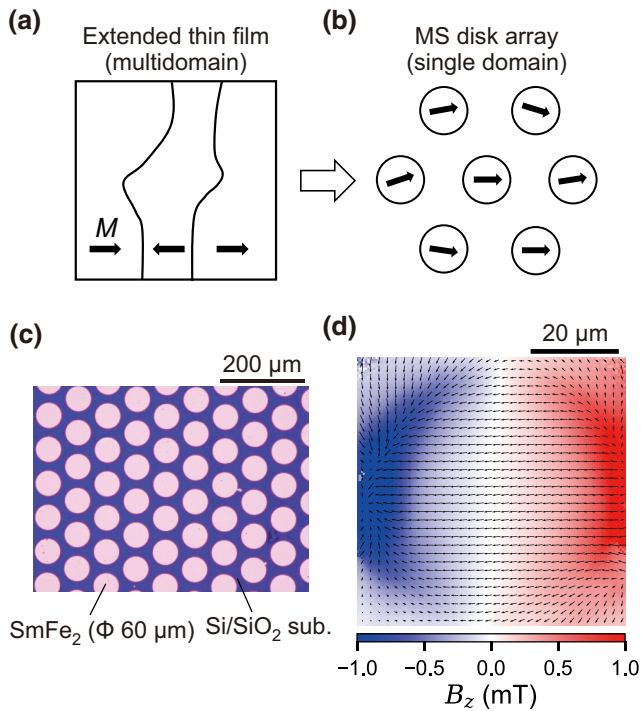


FIG. 5. (a),(b) Concept of pressure imaging. (a) Extended thin film has a multidomain structure, where the size of the domain is irregular, domain-wall motion can occur, and the domain structure is nonreproducible. (b) Single-domain MS disk array can realize more reliable pressure imaging. (c),(d) Experimental demonstration of the transformation of the MS disk into a single-domain magnet. (c) Optical image of the MS disk array. SmFe₂ deposited on the Si/SiO₂ substrate with a thickness of 100 nm is processed into disks with a diameter of 60 μm . Scale bar is 200 μm . (d) Measured magnetic field distribution on one MS disk. Color map represents the z component of the magnetic field and arrows represent the x - y component. Scale bar is 20 μm . Single-domain disk is successfully fabricated.

to ± 1 mT [Fig. 5(d)], which means that the pressure coefficient may increase.

V. CONCLUSION

We demonstrate the imaging of the magnetic response to external pressure using a MS–N– V hybrid structure. A pressure-induced change in the resonant frequency is imaged. Through widefield imaging, the pressure coefficients are found to be correlated with the multidomain structure of the MS layer, which must be considered in widefield pressure imaging. The values of the pressure coefficient are positive or negative in the domain and approximately zero on the domain wall. The highest pressure coefficient is observed in a domain, and the value is (8.2 ± 0.9) kHz kPa⁻¹, which is 550 times larger than that realized by a single structure of the N– V center. Moreover, we propose the approach of using microstructured

single-domain MS arrays to improve sensitivity and controllability and ensure an accurate calibration of pressure imaging. We fabricate a single-domain MS disk and discuss the potential of the MS–N– V hybrid structure to become one of the candidates for pressure imaging.

ACKNOWLEDGMENTS

This study is supported by the MEXT Quantum Leap Flagship Program (MEXT Q-LEAP) (Grant No. JPMXS0118067395) and JST SPRING (Grant No. JPMJSP2106).

APPENDIX A: WEIGHT CALIBRATION

We calibrate the weights using an electronic balance instead of the MS–N– V structure (Fig. 6). The measured weight increases monotonically with respect to the applied weight, with a root-mean-square error of $1\sigma = 2.1$ g. We use this value as the error in the weight. The error in the pressure is calculated assuming no error in the area where the pressure is applied.

APPENDIX B: OFFSET SUBTRACTION

The change in the resonant frequency observed outside SmFe₂ is considered as the offset (Fig. 7). Referring to the magnetic field image, the magnetic field is spatially distributed on SmFe₂ and nearly uniform outside SmFe₂ [Fig. 7(a)]. The uniformity of the magnetic field outside SmFe₂ indicates a sufficiently small stray field from SmFe₂. Therefore, pressure-induced changes in the resonant frequency are not expected outside SmFe₂.

However, in our experiments, pressure-dependent changes in the resonant frequency are observed, even outside SmFe₂ [Figs. 7(b) and 7(c)]. Its value is approximately 2.3 kHz kPa⁻¹, and it is spatially uniform. Although the reason for the offset remains unknown, we consider the

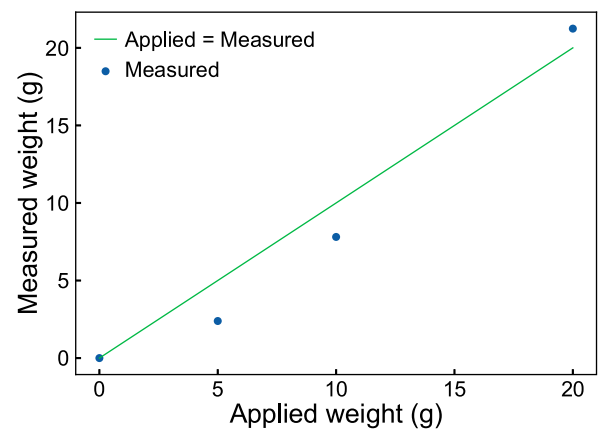


FIG. 6. Calibration of the weight. Horizontal axis represents the weight of the calibrated weight. Vertical axis represents the weight measured using an electronic balance.

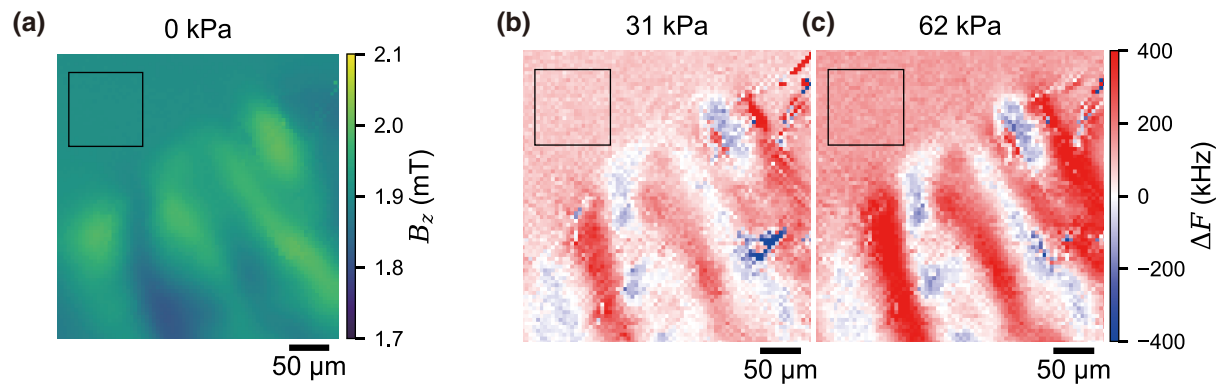


FIG. 7. (a) Magnetic field image and (b),(c) changes in the magnetic field with respect to pressure before subtracting the offset. Area in the black square is the region referred to as the offset. Scale bar is 50 μm .

change in the resonant frequency observed outside SmFe_2 to be the offset and subtract this value over the entire FOV.

- [1] F. Jelezko, T. Gaebel, I. Popa, A. Gruber, and J. Wrachtrup, Observation of Coherent Oscillations in a Single Electron Spin, *Phys. Rev. Lett.* **92**, 076401 (2004).
- [2] P. Neumann, J. Beck, M. Steiner, F. Rempp, H. Fedder, P. R. Hemmer, J. Wrachtrup, and F. Jelezko, Single-shot readout of a single nuclear spin, *Science* **329**, 542 (2010).
- [3] J. R. Maze, P. L. Stanwix, J. S. Hodges, S. Hong, J. M. Taylor, P. Cappellaro, L. Jiang, M. V. G. Dutt, E. Togan, A. S. Zibrov, A. Yacoby, R. L. Walsworth, and M. D. Lukin, Nanoscale magnetic sensing with an individual electronic spin in diamond, *Nature* **455**, 644 (2008).
- [4] J. M. Taylor, P. Cappellaro, L. Childress, L. Jiang, D. Budker, P. R. Hemmer, A. Yacoby, R. Walsworth, and M. D. Lukin, High-sensitivity diamond magnetometer with nanoscale resolution, *Nat. Phys.* **4**, 810 (2008).
- [5] D. Le Sage, K. Arai, D. R. Glenn, S. J. DeVience, L. M. Pham, L. Rahn-Lee, M. D. Lukin, A. Yacoby, A. Komeili, and R. L. Walsworth, Optical magnetic imaging of living cells, *Nature* **496**, 486 (2013).
- [6] M. W. Doherty, N. B. Manson, P. Delaney, F. Jelezko, J. Wrachtrup, and L. C. L. Hollenberg, The nitrogen-vacancy colour centre in diamond, *Phys. Rep.* **528**, 1 (2013).
- [7] M. W. Doherty, V. M. Acosta, A. Jarmola, M. S. J. Barson, N. B. Manson, D. Budker, and L. C. L. Hollenberg, Temperature shifts of the resonances of the NV^- center in diamond, *Phys. Rev. B* **90**, 041201(R) (2014).
- [8] F. Dolde, H. Fedder, M. W. Doherty, T. Nöbauer, F. Rempp, G. Balasubramanian, T. Wolf, F. Reinhard, L. C. L. Hollenberg, F. Jelezko, and J. Wrachtrup, Electric-field sensing using single diamond spins, *Nat. Phys.* **7**, 459 (2011).
- [9] M. S. J. Barson, P. Peddibhotla, P. Ovarthaiyapong, K. Ganesan, R. L. Taylor, M. Gebert, Z. Mielens, B. Koslowski, D. A. Simpson, L. P. McGuinness, J. McCallum, S. Prawer, S. Onoda, T. Ohshima, A. C. Bleszynski Jayich, F. Jelezko, N. B. Manson, and M. W. Doherty, Nanomechanical sensing using spins in diamond, *Nano Lett.* **17**, 1496 (2017).
- [10] S. Hsieh, P. Bhattacharyya, C. Zu, T. Mittiga, T. J. Smart, F. Machado, B. Kobrin, T. O. Höhn, N. Z. Rui, M. Kamrani, S. Chatterjee, S. Choi, M. Zaletel, V. V. Struzhkin, J. E. Moore, V. I. Levitas, R. Jeanloz, and N. Y. Yao, Imaging stress and magnetism at high pressures using a nanoscale quantum sensor, *Science* **366**, 1349 (2019).
- [11] M. W. Doherty, V. V. Struzhkin, D. A. Simpson, L. P. McGuinness, Y. Meng, A. Stacey, T. J. Karle, R. J. Hemley, N. B. Manson, L. C. L. Hollenberg, and S. Prawer, Electronic Properties and Metrology Applications of the Diamond NV^- Center under Pressure, *Phys. Rev. Lett.* **112**, 047601 (2014).
- [12] V. Ivády, T. Simon, J. R. Maze, I. A. Abrikosov, and A. Gali, Pressure and temperature dependence of the zero-field splitting in the ground state of NV^- centers in diamond: A first-principles study, *Phys. Rev. B* **90**, 235205 (2014).
- [13] G. Balasubramanian, I. Y. Chan, R. Kolesov, M. Al-Hmoud, J. Tisler, C. Shin, C. Kim, A. Wojcik, P. R. Hemmer, A. Krueger, T. Hanke, A. Leitenstorfer, R. Bratschitsch, F. Jelezko, and J. Wrachtrup, Nanoscale imaging magnetometry with diamond spins under ambient conditions, *Nature* **455**, 648 (2008).
- [14] P. Maletinsky, S. Hong, M. S. Grinolds, B. Hausmann, M. D. Lukin, R. L. Walsworth, M. Loncar, and A. Yacoby, A robust scanning diamond sensor for nanoscale imaging with single nitrogen-vacancy centres, *Nat. Nanotechnol.* **7**, 320 (2012).
- [15] L. M. Pham, D. Le Sage, P. L. Stanwix, T. K. Yeung, D. Glenn, A. Trifonov, P. Cappellaro, P. R. Hemmer, M. D. Lukin, H. Park, A. Yacoby, and R. L. Walsworth, Magnetic field imaging with nitrogen-vacancy ensembles, *New J. Phys.* **13**, 045021 (2011).
- [16] D. A. Simpson, J.-P. Tetienne, J. M. McCoe, K. Ganesan, L. T. Hall, S. Petrou, R. E. Scholten, and L. C. L. Hollenberg, Magneto-optical imaging of thin magnetic films using spins in diamond, *Sci. Rep.* **6**, 22797 (2016).
- [17] G. Popescu, K. Park, M. Mir, and R. Bashir, New technologies for measuring single cell mass, *Lab Chip* **14**, 646 (2014).
- [18] K. Park, L. J. Millet, N. Kim, H. Li, X. Jin, G. Popescu, N. R. Aluru, K. J. Hsia, and R. Bashir, Measurement of

- adherent cell mass and growth, *Proc. Natl. Acad. Sci. U. S. A.* **107**, 20691 (2010).
- [19] B. Lee, J.-Y. Oh, H. Cho, C. W. Joo, H. Yoon, S. Jeong, E. Oh, J. Byun, H. Kim, S. Lee, J. Seo, C. W. Park, S. Choi, N.-M. Park, S.-Y. Kang, C.-S. Hwang, S.-D. Ahn, J.-I. Lee, and Y. Hong, Ultraflexible and transparent electroluminescent skin for real-time and super-resolution imaging of pressure distribution, *Nat. Commun.* **11**, 663 (2020).
- [20] T. H. Nguyen, M. E. Kandel, M. Rubessa, M. B. Wheeler, and G. Popescu, Gradient light interference microscopy for 3D imaging of unlabeled specimens, *Nat. Commun.* **8**, 210 (2017).
- [21] J. Cai, F. Jelezko, and M. B. Plenio, Hybrid sensors based on colour centres in diamond and piezoactive layers, *Nat. Commun.* **5**, 4065 (2014).
- [22] M. Tomita, Y. Ishitani, S. Ishiyama, Y. Takamura, and S. Nakagawa, in 2018 IEEE International Magnetism Conference (INTERMAG) (IEEE, 2018), pp. 1–1.
- [23] K. Tahara, H. Ozawa, T. Iwasaki, N. Mizuochi, and M. Hatano, Quantifying selective alignment of ensemble nitrogen-vacancy centers in (111) diamond, *Appl. Phys. Lett.* **107**, 193110 (2015).
- [24] H. Ozawa, K. Tahara, H. Ishiwata, M. Hatano, and T. Iwasaki, Formation of perfectly aligned nitrogen-vacancy-center ensembles in chemical-vapor-deposition-grown diamond (111), *Appl. Phys. Express* **10**, 045501 (2017).
- [25] B. D. Cullity and C. D. Graham, *Introduction to Magnetic Materials* (John Wiley & Sons, Inc, Hoboken, NJ, USA, 2008).
- [26] A. Gruber, A. Dräbenstedt, C. Tietz, L. Fleury, J. Wrachtrup, and C. von Borczyskowski, Scanning confocal optical microscopy and magnetic resonance on single defect centers, *Science* **276**, 2012 (1997).
- [27] J. H. N. Loubser and J. A. van Wyk, Electron spin resonance in the study of diamond, *Rep. Prog. Phys.* **41**, 1201 (1978).
- [28] N. B. Manson, J. P. Harrison, and M. J. Sellars, Nitrogen-vacancy center in diamond: Model of the electronic structure and associated dynamics, *Phys. Rev. B* **74**, 104303 (2006).
- [29] L. Robledo, H. Bernien, T. Van Der Sar, and R. Hanson, Spin dynamics in the optical cycle of single nitrogen-vacancy centres in diamond, *New J. Phys.* **13**, 025013 (2011).
- [30] Y. Takamura, Y. Shuto, S. Yamamoto, H. Funakubo, M. K. Kurosawa, S. Nakagawa, and S. Sugahara, Inverse-magnetostriction-induced switching current reduction of STT-MTJs and its application for low-voltage MRAM, *Solid-State Electron.* **128**, 194 (2017).
- [31] T. Tsuji, H. Ishiwata, T. Sekiguchi, T. Iwasaki, and M. Hatano, High growth rate synthesis of diamond film containing perfectly aligned nitrogen-vacancy centers by high-power density plasma CVD, *Diamond Relat. Mater.* **123**, 108840 (2022).
- [32] S. Steinert, F. Dolde, P. Neumann, A. Aird, B. Naydenov, G. Balasubramanian, F. Jelezko, and J. Wrachtrup, High sensitivity magnetic imaging using an array of spins in diamond, *Rev. Sci. Instrum.* **81**, 043705 (2010).
- [33] E. V. Levine, M. J. Turner, P. Kehayias, C. A. Hart, N. Langellier, R. Trubko, D. R. Glenn, R. R. Fu, and R. L. Walsworth, Principles and techniques of the quantum diamond microscope, *Nanophotonics* **8**, 1945 (2019).
- [34] S. Felton, A. M. Edmonds, M. E. Newton, P. M. Martineau, D. Fisher, D. J. Twitchen, and J. M. Baker, Hyperfine interaction in the ground state of the negatively charged nitrogen vacancy center in diamond, *Phys. Rev. B* **79**, 075203 (2009).
- [35] B. S. Reddy and B. N. Chatterji, An FFT-based technique for translation, rotation, and scale-invariant image registration, *IEEE Trans. Image Process.* **5**, 1266 (1996).
- [36] H. Chen, S. Asif, M. Whalen, J. Támara-Isaza, B. Luetke, Y. Wang, X. Wang, M. Ayako, S. Lamsal, A. F. May, M. A. McGuire, C. Chakraborty, J. Q. Xiao, and M. J. H. Ku, Revealing room temperature ferromagnetism in exfoliated Fe₅GeTe₂ flakes with quantum magnetic imaging, *2D Mater.* **9**, 025017 (2022).
- [37] F. Casola, T. van der Sar, and A. Yacoby, Probing condensed matter physics with magnetometry based on nitrogen-vacancy centres in diamond, *Nat. Rev. Mater.* **3**, 17088 (2018).
- [38] G. Podaru and V. Chikan, in *Magnetic Nanomaterials: Applications in Catalysis and Life Sciences*, edited by S. H. Bossmann, H. Wang (The Royal Society of Chemistry, Cambridge, 2017), Chap. 1, p. 1.